Supporting Information

Global and time-resolved monitoring of crop photosynthesis with chlorophyll fluorescence

Luis Guanter[1], Yongguang Zhang[1], Martin Jung[2], Joanna Joiner[3], Maximilian Voigt[1], Joseph A. Berry[4], Christian Frankenberg[5], Alfredo Huete[6], Pablo Zarco-Tejada[7], Jung-Eun Lee[8], M. Susan Moran[9], Guillermo Ponce-Campos[9], Christian Beer[10], Gustavo Camps-Valls[11], Nina Buchmann[12], Damiano Gianelle[13], Katja Klumpp[14], Alessandro Cescatti[15], John M. Baker[16], and Timothy J. Griffis[17]

[1]Institute for Space Sciences, Freie Universität Berlin, Germany
[2]Department for Biogeochemical Systems, Max Planck Institute for Biogeochemistry, Jena, Germany
[3]NASA Goddard Space Flight Center, Greenbelt, MD, USA
[4]Department of Global Ecology, Carnegie Institution for Science, Stanford, CA, USA
[5]Jet Propulsion Laboratory, California Institute of Technology, Pasadena, CA, USA
[6]Plant Functional Biology and Climate Change Cluster, University of Technology Sydney, Australia
[7]Instituto de Agricultura Sostenible (IAS), CSIC, Córdoba, Spain
[8]Geological Sciences, Brown University, Providence, RI, USA
[9]USDA ARS Southwest Watershed Research Center, Tucson, AZ, USA
[10]Department of Applied Environmental Science (ITM) and Bert Bolin Centre for Climate Research, Stockholm University, Stockholm, Sweden
[11]Image Processing Laboratory, Universitat de València, Spain
[12]ETH Zurich, Agricultural Sciences, Zurich, Switzerland
[13]Sustainable Agro-ecosystems and Bioresources Dept., Research and Innovation Centre, Fondazione E. Mach, Italy
[14]Grassland Ecosystem Research Unit, INRA, Clermont-Ferrand, France
[15]European Commission, JRC, Institute for Environment and Sustainability, Ispra, Italy
[16]USDA ARS Soil and Water Management Research, St Paul, MN, USA
[17]Department of Soil, Water, and Climate, University of Minnesota, St Paul, MN, USA

Contents

1 SIF retrievals

We use SIF data derived from spectral radiance measurements by the GOME-2 instrument onboard the Eumetsat's MetOp-A platform launched in October 2006. Details can be found in [1]. GOME-2 measures in the 240–790 nm spectral range with relatively high spectral resolution (∼0.2–0.4 nm), signal-to-noise ratio (∼1000–2000), and a footprint size of 40×80 km^2. SIF retrievals are performed in the 715–758 nm spectral window overlapping the second peak of the SIF emission. The retrieval method disentangles SIF from the spectral signals of atmospheric absorption and scattering and of surface reflectance which affect the measured top-of-atmosphere radiance. The retrievals are quality-filtered and binned in a 0.5° lat-lon grid. GOME-2 data between 2007 and 2011 have been used in this work.

Fig. S1 presents SIF retrievals from GOME-2 and GOSAT's Fourier Transform Spectrometer (FTS) data over the northern temperate region. NDVI from the MODIS MOD13C2 product is also shown for reference. The retrieval approach applied to the GOSAT data is described in Guanter et al. [2]. The retrieval of SIF from GOSAT data is much simpler than that for GOME-2 thanks to the very high spectral resolution of the GOSAT's FTS (∼0.025 nm), which allows to use narrow fitting windows (hence simpler modeling of the background surface reflectance) and to resolve individual solar Fraunhofer lines (i.e. free from contamination by atmospheric absorption, mostly O_2 in this spectral range). GOSAT/FTS measurements consist of round field-of-views of about 10 km diameter separated by hundreds of kilometers. The random component of the single-retrieval error is high, in the range of 50–100%, due to the narrow fitting window used for the retrieval and the relatively low signal-to-noise ratio (∼100–300) of the FTS. Global composites of monthly SIF from GOSAT retrievals are typically produced by averaging in 2° gridboxes. Despite the noise and the low spatial resolution of the GOSAT SIF composites, we consider them to be highly accurate (free from systematic errors) due to the simplicity of the retrieval approach based on narrow fitting windows and solely Fraunhofer lines. Therefore,

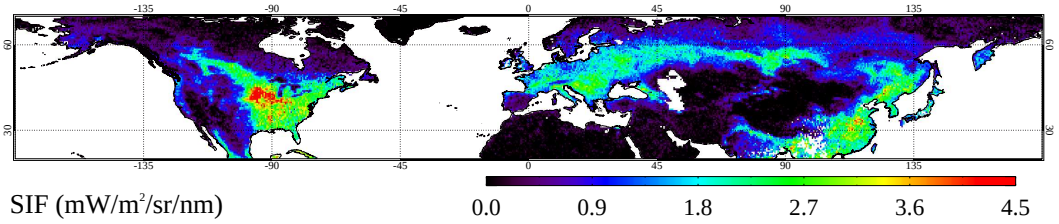

(a) SIF GOME-2, July 2009, 0.5° grid, 715–758 nm, ∼9:30h local time overpass

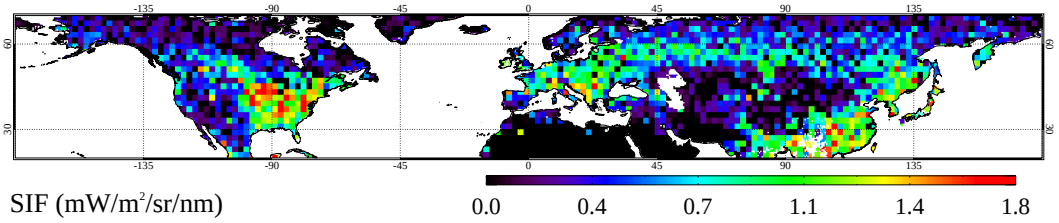

(b) SIF GOSAT, July 2009, 2° grid, 757 nm, ∼13h local time overpass

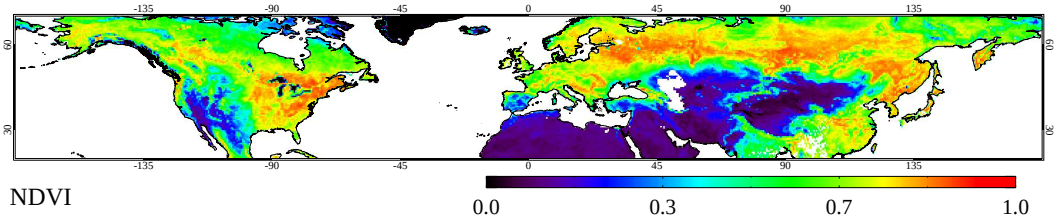

(c) NDVI, July 2009, 0.5° grid (MODIS MOD13C2)

Fig. S 1: Monthly composites (July 2009) of SIF retrievals from GOSAT/FTS and MetOp-A/GOME-2 measurements. NDVI from the MODIS MOD13C2 product is also shown for reference. GOME-2 retrievals are for a spectral fitting window centered around 740 nm (715–758 nm) and are gridded in 0.5° cells, whereas GOSAT retrievals are for a narrow window at 757 nm and are gridded in 2° cells.

the good comparison between the spatial patterns in the GOSAT and the GOME-2 SIF supports the consistency of the GOME-2 SIF data used in this work, and in particular of the outstanding SIF levels observed at the Midwest US in the GOME-2 data (Fig. 1–2 of the main text). Slight differences in the spatial patterns of GOSAT and GOME-2 SIF can be explained by the lower precision of the GOSAT retrievals, which leads to noisier SIF composites, and the different overpass times (morning for MetOp-A, noon for GOSAT) which makes the latitudinal differences in the solar flux received in the north and the south to be greater for GOSAT than for GOME-2. The absolute SIF values differ for GOME-2 and GOSAT-FTS because of the different retrieval wavelengths and instantaneous illumination fluxes associated to the overpass time of each satellite.

2 Model-based GPP data

We have used global GPP estimates from ensembles of data-driven and process-based models as follows:

- **Data-driven models** are based on the calculation of GPP with empirical and semi-empirical relationships between GPP and a series of diagnostic variables (e.g. vegetation parameters such as the fraction of absorbed photosynthetically active radiation and meteorological variables such as short-wave radiation or vapor pressure deficit). As representative of state-of-the-art data-driven methods, we have used annual GPP estimates from 5 of the data-driven models described in Beer et al. [3], namely MTE1, MTE2, ANN, KGB and LUE. These models differ with each other in how the relationship between the diagnostic variables and GPP is expressed.

  In addition, monthly GPP estimates from the MTE1 model, referred to as Max Planck Institute for Biogeochemistry (MPI-BGC) model [4] in the main text, and from the MODIS GPP model (MOD17) [5] are used in the comparison with flux tower GPP in Fig. 2 of the main text and Fig. S4, respectively. The MPI-BGC GPP data set is produced through the global upscaling of site measurements of carbon dioxide fluxes. This is based on a Model Tree Ensemble approach for a statistical formulation of the relationship between GPP and vegetation parameters derived from remote sensing data and meteorological variables from re-analysis products. MOD17 GPP is derived from a production-efficiency approach consisting in the formulation of GPP as the product of absorbed photosynthetically-active radiation derived from satellite and meteorological data and tabulated light use efficiency.

- **Process-based models** or dynamic global vegetation models (DGVMs), are based on mathematical representations of physiological and ecological mechanisms driving productivity among other vegetation responses. The DGVMs in our ensemble of process-based models are part of the Trendy activity[1] intended to intercompare *Trends in net land - atmosphere carbon exchange* over the period 1980–2010. We have use the CLM4C, CLM4CN, HYLAND, LPJ, LPJ-GUESS, OCN, Orichidee, SDGVM, TRIFFID, and VEGAS models. Model outputs were available at different spatial resolutions. The data from the LPJ, LPJ-GUESS, Orchidee and VEGAS models were simulated at $0.5^\circ \times 0.5^\circ$ resolution, CLM4C and CLM4CN at $2.5^\circ \times 1.875^\circ$, and OCN, TRIFFID and HYLAND other at $3.75^\circ \times 2.5^\circ$. All 10 models have been resampled to the 0.5° grid used for the SIF measurements, the data-driven model ensemble and the NPP inventories.

Fig. S2 shows the median and the standard deviation of the annual GPP from the 5 data-driven models from Beer et al. [3] and the 10 process-based Trendy models from Piao et al. [6], Sitch et al. [7] that we have used in this study. The median of the annual GPP from the two model ensembles shows similar absolute values, although there are some spatial differences, especially in North America. The spread of GPP estimates is significantly smaller for the data-driven models than for the process-based models.

[1] `http://dgvm.ceh.ac.uk/node/9`

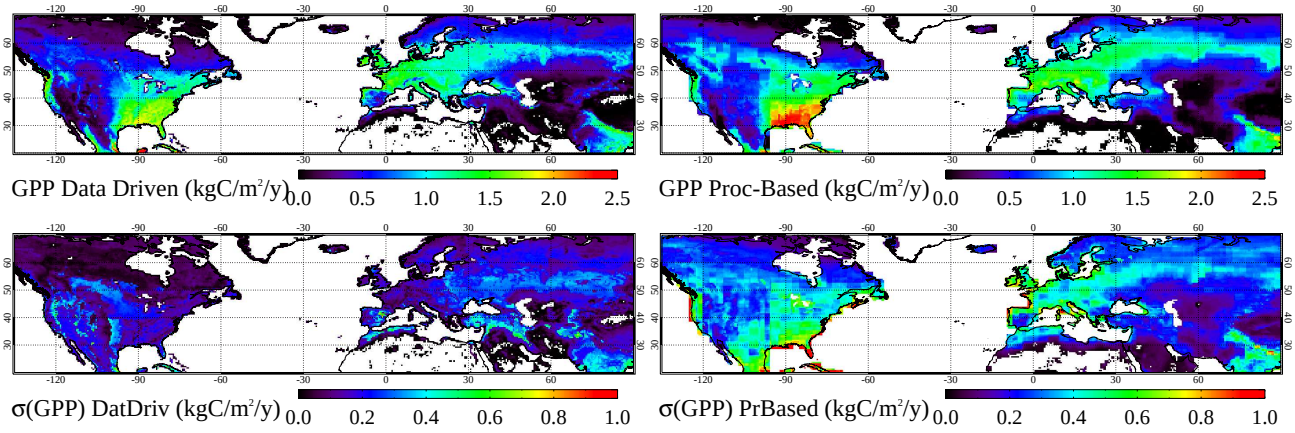

Fig. S 2: Median (top row) and mean absolute deviation (bottom row) of annual GPP estimates in North America and Western Europe from the data-driven and process-based model ensembles used in this work. Details about each model ensemble can be found in Beer et al. [3] and Piao et al. [6], Sitch et al. [7], respectively.

3 Comparison of flux tower-based GPP with model GPP, SIF and vegetation indices

We used fourteen eddy flux sites from the FLUXNET network [8] (Table S1). Six of these sites are located in crop fields in the US Corn Belt. The remaining eight stations include five crop sites and three grassland sites located across Europe. Sites have been selected on the basis of landscape homogeneity in the GOME-2 grid and on data availability in the period of interest (2007–2011). To determine landscape homogeneity, we used land cover type data from the MODIS Collection 5 MCD12C1 product (Friedl et al. [9]) and EVI data from the MODIS MOD13C2 product (Huete et al. [10]), both with spatial resolution of 0.05°. For a site to be selected for the study, the dominant vegetation cover type at the flux site (either cropland or grassland) must represent more than 60% of the GOME-2 pixel area, and the standard deviation of the EVI must be less than 0.10 (see Table S1). We used the Level 4 data product for the six US crop sites from the AmeriFlux website[2], and from the GHG-Europe database[3] for the eight Europe sites. Monthly GPP values were used in our investigation. GPP is estimated by partitioning the observed net flux into GPP and ecosystem respiration as discussed in Reichstein et al. [11] and Papale et al. [12].

For each site, SIF was extracted based on the coordinates of the flux tower, and averaged to monthly means when at least 5 SIF retrievals were available. Three US crop sites (US-IB1, Ne2-3, Ro1) are very close to big cities. To avoid signal contamination from urban areas, we extracted SIF from a nearby pixel fulfilling the homogeneity criteria. Given that flux measurements are usually representative of a large area in homogeneous landscapes (i.e., US-IB1 is representative of central Illinois), we assumed that SIF (or EVI and NDVI) from nearby grid boxes can represent the footprint of the flux towers. Monthly SIF

[2] http://ameriflux.ornl.gov/

[3] http://www.europe-fluxdata.eu/

and GPP were averaged over the 2007–2011 observation period for each month to minimize uncertainties due to the different spatial scales of the SIF retrievals and the flux tower data. This uncertainties occur because both corn and soybean fields exist in the GOME-2 footprint for the US flux sites. A mixed signal of corn and soybean is therefore sampled by the GOME-2 footprint, while the eddy covariance tower measured flux either from corn or soybean for each year. Multi-year averaging may help reduce this mismatch.

Table S 1: Details of the flux tower sites used in this study. LC stands for Land Cover class, max(LC) stands for the percent of dominant vegetation cover within the GOME-2 pixel, EVI is the MODIS Enhanced Vegetation Index, and σ(EVI) represents the standard deviation of EVI within the GOME-2 pixel.

Site ID	Country	Lat. (°)	Lon. (°)	IGBP class	Study period	max(LC) (%)	mean EVI	σ EVI	Vegetation type or crop rotations	Reference
US-Bo1	USA	40.00	-88.29	CRO	2007	0.98	0.55	0.04	Corn	Ryu et al. [13]
US-IB1	USA	41.85	-88.22	CRO	2007–2009	0.98	0.44	0.08	Soybean/Corn/Soyb.	Allison et al. [14]
US-Ne2	USA	41.16	-96.47	CRO	2007–2010	0.94	0.56	0.07	Corn/Soybean/Corn/Corn	Suyket et al. [15]
US-Ne3	USA	41.17	-96.43	CRO	2007–2010	0.95	0.57	0.07	Corn/Soybean/Corn/Soyb.	Suyker et al. [15]
US-Ro1	USA	44.71	-93.09	CRO	2007–2010	1.00	0.49	0.10	Corn/Soybean/Corn/Soyb.	Griffis et al. [16]
US-SFP	USA	43.24	-96.90	CRO	2007–2009	1.00	0.55	0.03	Continuous corn	–
DE-Gri	Germany	50.94	13.51	GRA	2007–2010	0.58	0.44	0.04	Permanent grassland	Hussain et al. [17]
FR-Lq1	France	45.64	2.73	GRA	2007–2010	0.79	0.57	0.04	Permanent grassland	Klumpp et al. [18]
HU-Bug	Hungary	46.69	19.60	GRA	2007–2008	0.94	0.35	0.03	Permanent grassland	Naggy et al. [19]
BE-Lon	Belgium	50.55	4.74	CRO	2007–2010	0.71	0.49	0.07	Winter wheat/sugar beet/ /winter wheat/seed potato	Aubinet et al. [20]
CH-Oe2	Switzerland	47.28	7.73	CRO	2007–2009	0.71	0.50	0.05	Winter wheat/rapeseed/ /winter wheat	Dietiker et al. [21]
DE-Geb	Germany	51.10	10.91	CRO	2007–2010	0.97	0.46	0.08	Winter wheat/rapeseed/ /barley/sugar beet	Kutsch et al. [22]
DE-Seh	Germany	50.87	6.44	CRO	2007–2010	0.60	0.45	0.07	Winter wheat/winter wheat/ /sugar beet/winter wheat	Schmidt et al. [23]
IT-Cas	Italy	45.06	8.66	CRO	2007–2010	0.97	0.43	0.09	Continuous paddy rice	Skiba et al. [24]

Reflectance-based vegetation indices derived from satellite observations [e.g. 10, 25] provide information about vegetation *greenness* (i.e. a combination of biomass, chlorophyll content and structural effects) and have also been reported to be good indicators of gross primary production [e.g. 26]. The data-driven GPP models combine these reflectance-based proxies for green biomass and canopy light interception with meteorological inputs modulating photosynthesis at the ecosystem scale.

To complete the comparison of model GPP with fluorescence and tower-based GPP discussed in the main text, we have also analyzed the relationship between flux tower GPP and the normalized difference vegetation index (NDVI) [27], the enhanced vegetation index (EVI) [10], both extracted from the MOD13C2 product, and the MERIS terrestrial chlorophyll index (MTCI) [28]. The NDVI is the most widely used vegetation index in the last decades. The EVI is a modification of the NDVI intended to improve the response of the NDVI for high green biomass levels and to reduce the sensitivity to atmospheric effects. The MTCI is designed to provide a high sensitivity to chlorophyll content through the sampling of the so-called red-edge window between the red and the near-infrared spectral regions.

Fig. S3 displays maps of the EVI, NDVI and MTCI for July 2009 and the same area as the GPP and SIF maps shown in Fig. 2 of the main text (please, note that maximum monthly values instead of July values are plotted in Fig. 2 of the main text, so this comparison is only approximate). The data-driven GPP from the MODIS MOD17 product is also shown. The NDVI appears to be close to saturation in the most densely vegetated areas of North America and Europe. This is not happening for the EVI, which shows a somewhat higher signal in the midwest and the east coast of the US than in Europe, in line with the spatial patterns of SIF and GPP MPI-BGC (Fig. 2 of the main text). No significant differences between Europe and the US are observed in the MOD17 GPP data. On the other hand, the spatial patterns of the MTCI at the US Corn Belt are the most similar ones to those of SIF. This could be due to the fact that both SIF and the MTCI are most sensitive to canopy chlorophyll content for the high levels of leaf-area index found at the peak of the growing season for the corn and soybean crops in the US Corn Belt.

The same three indices have been compared with flux tower-based GPP estimates as we have done with MPI-BGC GPP, process-based GPP from the Trendy models and SIF in Fig. 3 of the main text. Results are shown in Fig. S4, in this case also including the European crop sites not included in Fig. 3 of the main text. Points to be noted are (i) the relatively bad comparison between GPP and both EVI and NDVI for the US crops, (ii) the good correlation between EVI and GPP when the comparison is performed for all three biomes, (iii) the lower values of EVI and MTCI at the grasslands sites, which agrees with SIF and the tower-based GPP, but not with the data-driven GPP estimates, and (iv) the good performance of the MTCI to track GPP in the US crops. These results, together with the conclusions extracted from Fig. 3 of the main text, support our approach of selecting SIF as the best input to upscale cropland GPP from the tower footprint to the regional scale. The relationship GPP(SIF)=$-0.10+3.72\times$SIF) is used for this upscaling.

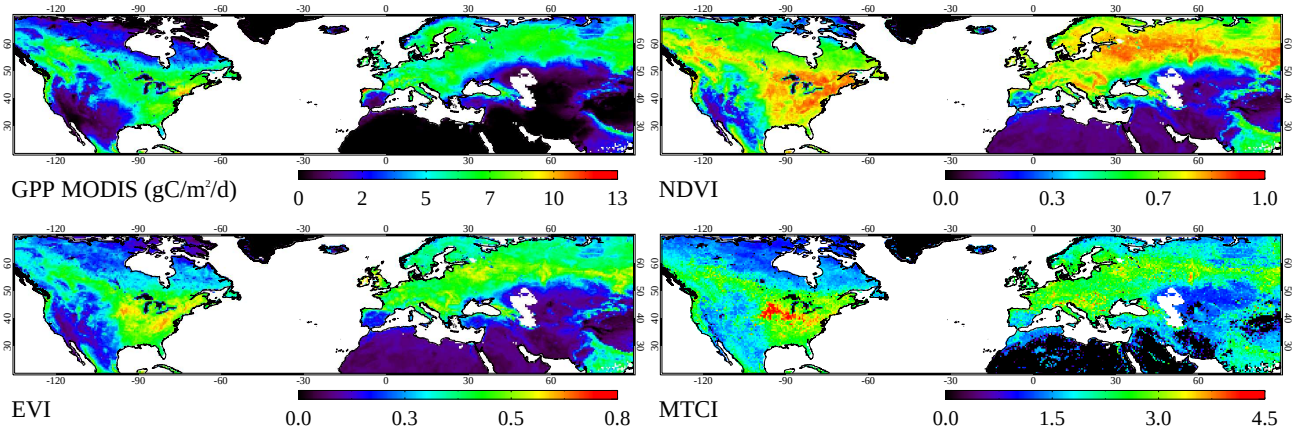

Fig. S 3: Maps of GPP from the MODIS MOD17 product, NDVI and EVI from the MODIS MOD13C2 product and the MERIS MTCI for July 2009 and the same region of the GPP and fluorescence maps displayed in Fig. 2 of the main text. Please, note that maximum monthly values instead of July values are plotted in Fig. 2 of the main text, so the comparison is only approximate.

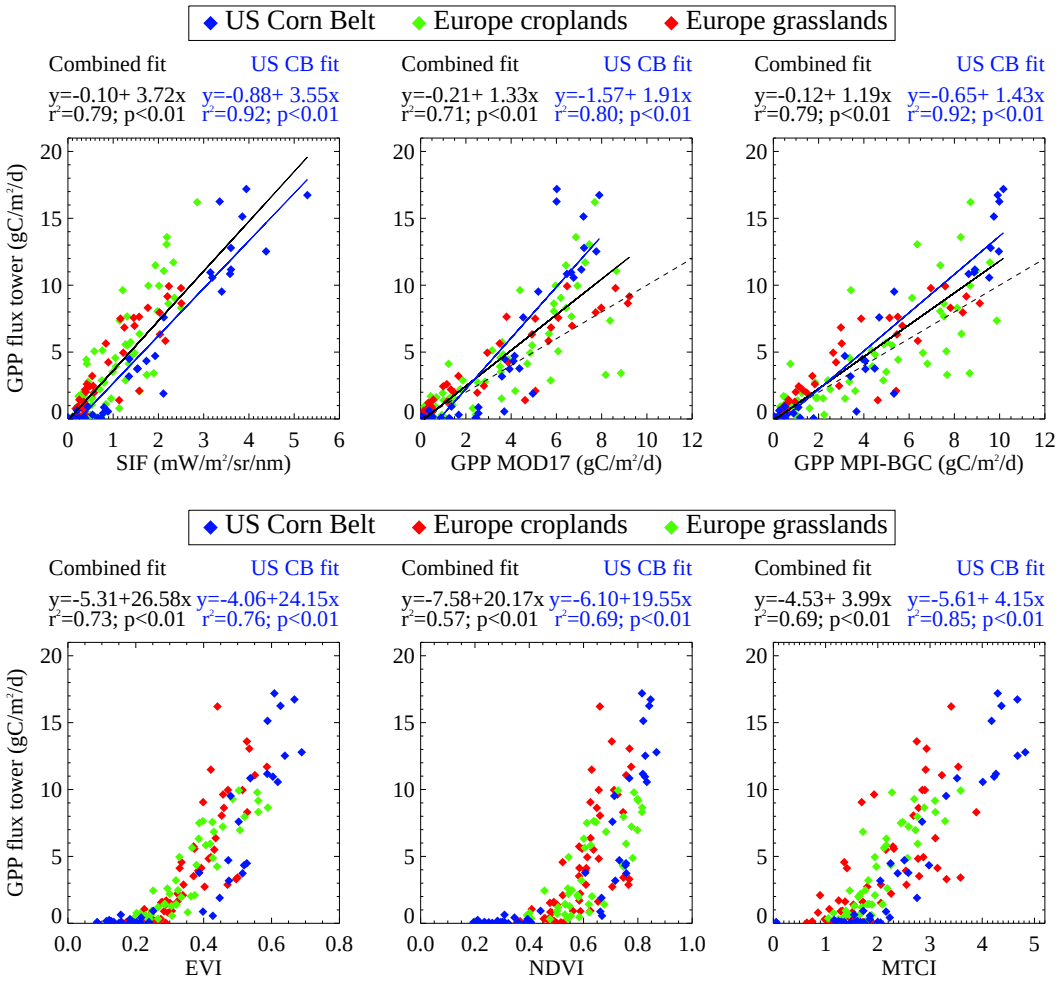

Fig. S 4: Similar to Fig. 3 of the main text but including the European cropland sites. Tower-based GPP is compared with SIF, GPP MPI-BGC and GPP MOD17 (top) and with EVI, NDVI and MTCI data (bottom).

4 Derivation of spatially-explicit crop GPP estimates

The monthly composites of SIF at 0.5° are scaled to GPP with the linear relationship derived from the comparison of SIF with flux tower-based GPP shown in Fig. S4a (GPP(SIF)=−0.10+3.72×SIF). Model-based GPP maps are generated as the median GPP per grid cell from the data-driven and process-based model ensembles described before. We have estimated crop GPP from the total GPP in the grid box by multiplying the total GPP by the fraction of cropland area in the gridbox described in Ramankutty et al. [29] and downloadable from `http://www.geog.mcgill.ca/~nramankutty/Datasets/Datasets.html`. As a result, we obtain the cropland GPP per unit total area, as shown in Fig. 6a of the main text. Comparison of annual, area-integrated crop GPP estimated from SIF and the data-driven and process-based models are provided in Table S2.

Table S 2: Annual, area-integrated GPP estimates over the US Corn Belt (35–50°N, -105–80°E), Western Europe (35–55°N, -10–25°E), India (23–33°N, 70–90°E), China (30–49°N, 110–135°E), South America (−40–−20°N, −45–−70°E), and the globe from the median of the data-driven and process-based biogeochemistry model ensembles and the scaled SIF. These regions match those used to produce Fig. 7 of the main text. Relative ΔGPP is calculated as SIF-based GPP minus model GPP over model GPP. Uncertainties are derived from the standard deviation of the ensembles in the case of the GPP models and from the errors in the slope and intercept in the linear regression in Fig. S4a for the scaled SIF.

	Crop GPP (PgC y^{-1})					
	US CB	**WestEur**	**India**	**China**	**SouthAm**	**Global**
GPP(Data-Driven)	1.1±0.2	1.3±0.3	0.8±0.3	0.73±0.16	0.95±0.15	17±4
GPP(Proc.-based)	1.3±0.5	1.5±0.6	0.9±0.4	0.9±0.3	1.2±0.4	20±9
GPP(SIF)	1.54±0.06	1.30±0.05	1.23±0.06	0.90±0.05	0.81±0.04	17.0±0.2
ΔGPP(Data-Driven)	43%	0%	55%	24%	−14%	3%
ΔGPP(Proc.-based)	18%	−14%	39%	−1%	−38%	−12%
Crop area (10^6 km^2)	1.2	1.3	1.0	0.9	0.7	16.5

5 NPP data from agricultural inventories

The SIF- and model-based crop GPP estimates have been compared with crop net primary productivity (NPP) estimates derived from agricultural inventories to produce Fig. 5 of the main text. Large-scale NPP estimates have been provided by the agricultural inventory data sets described in USDA-NASS [30] and Monfreda et al. [31]. The USDA NPP inventory was estimated using a statistical method that includes factors for dry weight, harvest indices, and root:shoot ratios multiplied by yield data from the National Agricultural Statistics Service (NASS). This method has been documented and published by Hicke and Lobell [32], Hicke et al. [33], Prince et al. [34]. U.S. county-level estimates of croplands production (P, in units of $MgCy^{-1}$) dataset is available in `http://cdiac.ornl.gov/carbonmanagement/cropcarbon/`. Data from the three most recent years (2006–2008) was used for

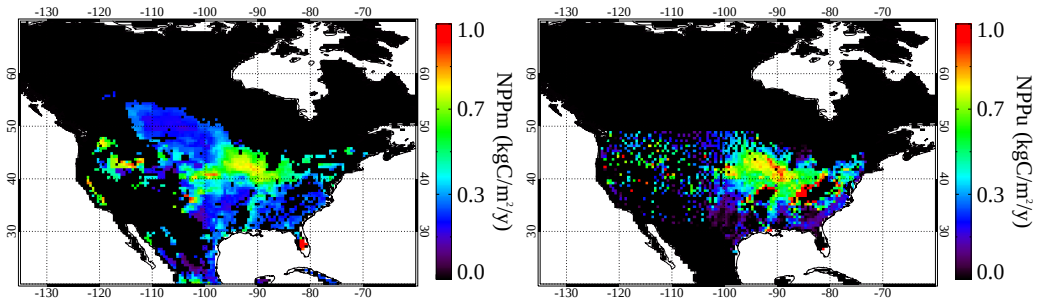

(a) Monfreda et al. (b) USDA

Fig. S 5: Crop NPP per harvested area in North America from the global inventory by Monfreda et al. for 2000 (a) and the USDA inventory (2006 and 2008) [33].

comparison. To derive the spatial distribution of cropland GPP, county-level NPP ($kgCm^{-2}y^{-1}$) was collocated in ArcGIS to a layer of the cultivated area of the US during 2008–2012. To compute NPP, we divide P by the total crop area of each county. The cultivated layer data is available from USDA NASS database at `http://www.nass.usda.gov/research/Cropland/Release/index.htm.`. Regarding the global inventory by Monfreda et al., it is based on the aggregation of 175 crop classes in a 5 min by 5 min grid following a method similar to the one proposed by Prince et al. [34] for the US. Monfreda et al. data corresponds to the year 2000.

Both USDA-NASS and Monfreda et al. NPP data sets are derived from the crop yields, and have units of per-harvested-areas (Fig. S5). NPP is converted from per-harvested-area to per-total-area units through the multiplication by the fraction of harvested area as described in Monfreda et al. (Fig. S6). The fraction of harvested area is calculated by summing the fraction of harvested area for each of the 175 crop classes considered by Monfreda et al. (data available from `http://www.geog.mcgill.ca/~nramankutty/Datasets/Datasets.html`).

The comparison of NPP from the USDA inventory with GPP from the SIF retrievals and the data-driven and process-based models for the US Western Corn Belt is shown in Fig. 5 of the main text. The same comparison for the NPP from Monfreda et al. for both the US and Western Europe is displayed in Fig S7.

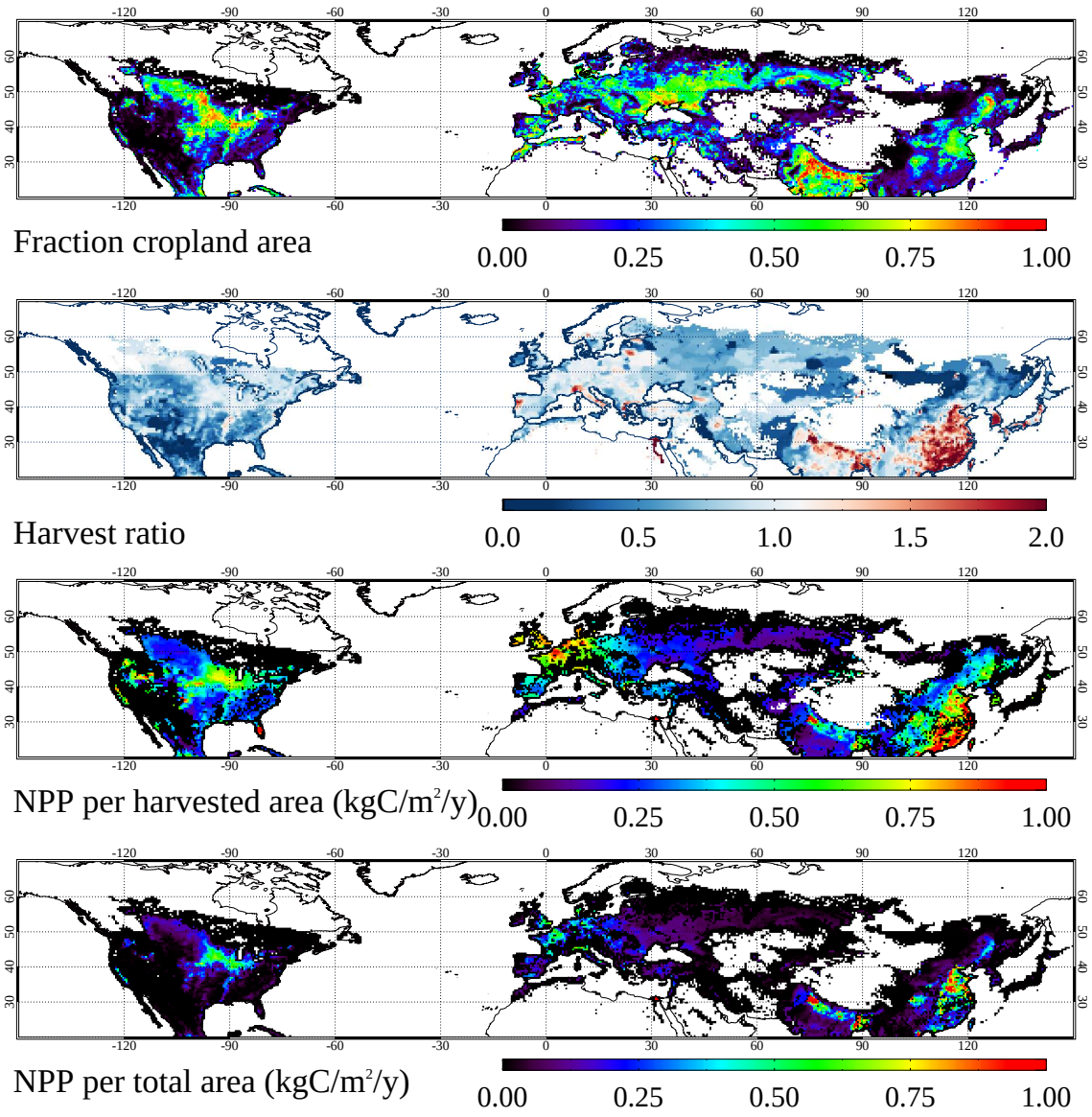

Fig. S 6: Cropland area and net primary production data sets from Ramankutty et al. [29] and Monfreda et al. [31] The fraction of cropland area expresses the ratio of cropland to total area in each 0.5° grid cell. The harvest ratio is the ratio of harvested-to-cropland area. The fraction of harvested area has been calculated from single fractions of harvested area provided by Monfreda et al. [31] for a total of 175 crop classes. The NPP per total area is calculated as the product of the original per-harvested-area NPP data from Monfreda et al. by the fraction of harvested area.

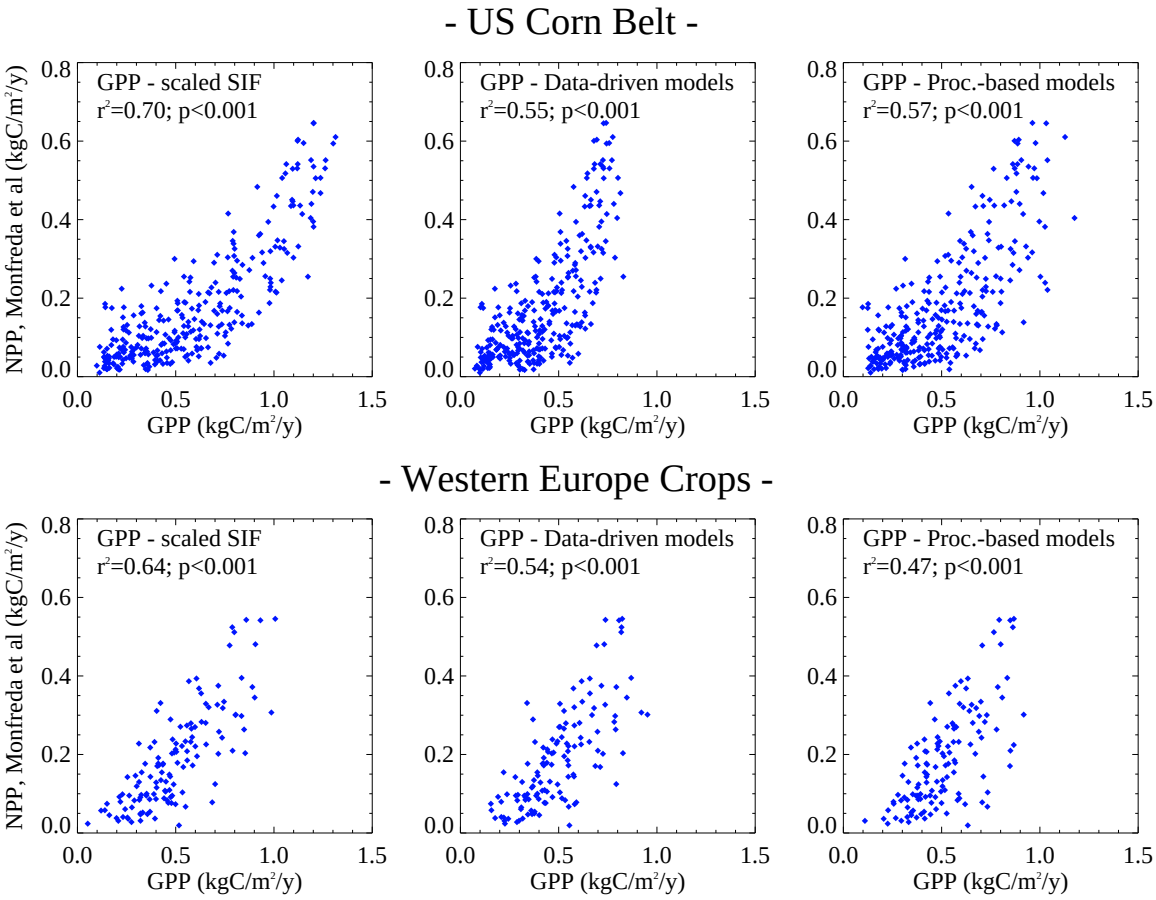

Fig. S 7: Same as Fig. 5 of the main text but for the NPP data set from the agricultural inventory by Monfreda et al. and showing results also for the Western Europe area (40–55°N, -5–15°E).

References

[1] J. Joiner, et al. Global monitoring of terrestrial chlorophyll fluorescence from moderate spectral resolution near-infrared satellite measurements: methodology, simulations, and application to GOME-2. *Atmospheric Measurement Techniques Discussions*, 6(2):3883–3930, 2013. doi: 10.5194/amtd-6-3883-2013.

[2] L. Guanter, et al. Retrieval and global assessment of terrestrial chlorophyll fluorescence from GOSAT space measurements. *Remote Sensing of Environment*, 121:236–251, 2012.

[3] C. Beer, et al. Terrestrial gross carbon dioxide uptake: Global distribution and covariation with climate. *Science*, 329(5993):834–838, 2010. doi: 10.1126/science.1184984.

[4] M. Jung, et al. Global patterns of land-atmosphere fluxes of carbon dioxide, latent heat, and sensible heat derived from eddy covariance, satellite, and meteorological observations. *Journal of Geophysical Research: Biogeosciences*, 116(G3):n/a–n/a, 2011. ISSN 2156-2202. doi: 10.1029/2010JG001566.

[5] S. W Running, et al. A Continuous Satellite-Derived Measure of Global Terrestrial Primary Production. *BioScience*, 54(6):547–560, 2004.

[6] S. Piao, et al. Evaluation of terrestrial carbon cycle models for their response to climate variability and to CO2 trends. *Global Change Biology*, 19(7):2117–2132, 2013.

[7] S. Sitch, et al. Trends and drivers of regional sources and sinks of carbon dioxide over the past two decades. *Biogeosciences Discussions*, 10(12):20113–20177, 2013. doi: 10.5194/bgd-10-20113-2013.

[8] D Baldocchi, et al. FLUXNET: A new tool to study the temporal and spatial variability of ecosystem-scale carbon dioxide, water vapor, and energy flux densities. *Bulletin of the American Meteorological Society*, 82(11):2415–2434, NOV 2001. ISSN 0003-0007.

[9] M. A. Friedl, et al. {MODIS} collection 5 global land cover: Algorithm refinements and characterization of new datasets. *Remote Sensing of Environment*, 114(1):168 – 182, 2010. ISSN 0034-4257. doi: http://dx.doi.org/10.1016/j.rse.2009.08.016.

[10] A Huete, et al. Overview of the radiometric and biophysical performance of the modis vegetation indices. *Remote Sensing of Environment*, 83(1-2):195 – 213, 2002. ISSN 0034-4257. doi: 10.1016/S0034-4257(02)00096-2.

[11] M. Reichstein, et al. On the separation of net ecosystem exchange into assimilation and ecosystem respiration: review and improved algorithm. *Global Change Biology*, 11(9):1424–1439, 2005. ISSN 1365-2486. doi: 10.1111/j.1365-2486.2005.001002.x.

[12] D. Papale, et al. Towards a standardized processing of net ecosystem exchange measured with eddy covariance technique: algorithms and uncertainty estimation. *Biogeosciences*, 3(4):571–583, 2006. doi: 10.5194/bg-3-571-2006.

[13] Y. Ryu, et al. On the temporal upscaling of evapotranspiration from instantaneous remote sensing measurements to 8-day mean daily-sums. *Agricultural and Forest Meteorology*, 152(0):212 – 222, 2012. ISSN 0168-1923. doi: http://dx.doi.org/10.1016/j.agrformet.2011.09.010.

[14] V. J. Allison, et al. Changes in soil microbial community structure in a tallgrass prairie chronosequence. *Soil Science Society of America Journal*, 69(5):1412–1421, SEP-OCT 2005. ISSN 0361-5995. doi: {10.2136/sssaj2004.0252}.

[15] A. E. Suyker, et al. Gross primary production and ecosystem respiration of irrigated maize and irrigated soybean during a growing season. *Agricultural and Forest Meteorology*, 131(34):180 – 190, 2005. ISSN 0168-1923. doi: http://dx.doi.org/10.1016/j.agrformet.2005.05.007.

[16] T. J. Griffis, et al. Direct measurement of biosphere-atmosphere isotopic co2 exchange using the eddy covariance technique. *Journal of Geophysical Research: Atmospheres*, 113(D8):n/a–n/a, 2008. ISSN 2156-2202. doi: 10.1029/2007JD009297.

[17] M. Z. Hussain, et al. Summer drought influence on CO2 and water fluxes of extensively managed grassland in Germany. *Agriculture Ecosystems & Environment*, 141(1-2):67–76, APR 2011. ISSN 0167-8809. doi: {10.1016/j.agee.2011.02.013}.

[18] K. Klumpp, et al. Long-term impacts of agricultural practices and climatic variability on carbon storage in a permanent pasture. *Global Change Biology*, 17(12):3534–3545, 2011. ISSN 1365-2486. doi: 10.1111/j.1365-2486.2011.02490.x.

[19] Z. Nagy, et al. Some preliminary results of the hungarian grassland ecological research: Carbon cycling and greenhouse gas balances under changing. *Cereal Research Communications*, 33(1): 279–281, 2005.

[20] M. Aubinet, et al. Carbon sequestration by a crop over a 4-year sugar beet/winter wheat/seed potato/winter wheat rotation cycle. *Agricultural and Forest Meteorology*, 149(34):407 – 418, 2009. ISSN 0168-1923. doi: http://dx.doi.org/10.1016/j.agrformet.2008.09.003.

[21] D. Dietiker, et al. Testing the ability of the {DNDC} model to predict {CO2} and water vapour fluxes of a swiss cropland site. *Agriculture, Ecosystems & Environment*, 139(3):396 – 401, 2010. ISSN 0167-8809. doi: http://dx.doi.org/10.1016/j.agee.2010.09.002.

[22] W.L. Kutsch, et al. The net biome production of full crop rotations in europe. *Agriculture, Ecosystems & Environment*, 139(3):336 – 345, 2010. ISSN 0167-8809. doi: http://dx.doi.org/10.1016/j.agee.2010.07.016.

[23] M. Schmidt, et al. The carbon budget of a winter wheat field: An eddy covariance analysis of seasonal and inter-annual variability. *Agricultural and Forest Meteorology*, 165(0):114 – 126, 2012. ISSN 0168-1923. doi: http://dx.doi.org/10.1016/j.agrformet.2012.05.012.

[24] U. Skiba, et al. Biosphereatmosphere exchange of reactive nitrogen and greenhouse gases at the nitroeurope core flux measurement sites: Measurement strategy and first data sets. *Agriculture, Ecosystems & Environment*, 133(34):139 – 149, 2009. ISSN 0167-8809. doi: http://dx.doi.org/10.1016/j.agee.2009.05.018.

[25] R.B. Myneni, et al. The interpretation of spectral vegetation indexes. *Geoscience and Remote Sensing, IEEE Transactions on*, 33(2):481–486, 1995. ISSN 0196-2892. doi: 10.1109/36.377948.

[26] D. A. Sims, et al. On the use of modis evi to assess gross primary productivity of north american ecosystems. *Journal of Geophysical Research: Biogeosciences*, 111(G4):n/a–n/a, 2006. ISSN 2156-2202. doi: 10.1029/2006JG000162. URL `http://dx.doi.org/10.1029/2006JG000162`.

[27] C. J. Tucker. Red and photographic infrared linear combinations for monitoring vegetation. *Remote Sensing of Environment*, 8:127–150, 1979.

[28] J. Dash et al. The MERIS terrestrial chlorophyll index. *International Journal of Remote Sensing*, 25:5003–5013, 2004.

[29] N. Ramankutty, et al. Farming the planet: 1. geographic distribution of global agricultural lands in the year 2000. *Global Biogeochemical Cycles*, 22(1), 2008. doi: 10.1029/2007GB002952.

[30] USDA-NASS. USDA National Agricultural Statistics Service Cropland Data Layer. Published crop-specific data layer [Online]. Technical report.

[31] C. Monfreda, et al. Farming the planet: 2. geographic distribution of crop areas, yields, physiological types, and net primary production in the year 2000. *Global Biogeochemical Cycles*, 22(1), 2008. doi: 10.1029/2007GB002947.

[32] J. A. Hicke et al. Spatiotemporal patterns of cropland area and net primary production in the central united states estimated from usda agricultural information. *Geophysical Research Letters*, 31(20):n/a–n/a, 2004. ISSN 1944-8007. doi: 10.1029/2004GL020927.

[33] J. A. Hicke, et al. Cropland Area and Net Primary Production Computed from 30 Years of USDA Agricultural Harvest Data. *Earth Interactions*, 8, 2004. ISSN 1087-3562.

[34] S. D. Prince, et al. Net primary production of US Midwest croplands from agricultural harvest yield data. *Ecological Applications*, 11(4):1194–1205, AUG 2001. ISSN 1051-0761. doi: {10.2307/3061021}.